The International Journal of Advanced Manufacturing Technology (2018) 96:871–879
https://doi.org/10.1007/s00170-018-1590-0

ORIGINAL ARTICLE

Adaptive process control of wire and arc additive manufacturing for fabricating complex-shaped components

Fang Li[1,2] · Shujun Chen[1,2] · Zhaoyang Wu[1,2] · Zhihong Yan[1,2]

Received: 4 April 2017 / Accepted: 9 January 2018 / Published online: 1 February 2018

Abstract
In wire and arc additive manufacturing (WAAM), it is crucial to maintain a constant travel speed in order to achieve a uniform bead morphology along the tool-path. However, this requirement is always violated in practice because the welding robot has to slow down when sharp corners with high curvatures are encountered so as to satisfy the dynamic constraint. The consequence is excessive fillings (i.e. humps) around these sharp corners, which not only increase the required post processing, but also prevent the continuation of the deposition process if the accumulated errors in the build direction become too large. This issue greatly limits the application of WAAM in the fabrication of complex-shaped components. In this paper, an adaptive process control scheme (APCS) capable of guaranteeing a uniform bead morphology while still respecting the dynamic constraint is proposed. First, the APCS divides the tool-path into several segments depending on whether they contain sharp corners. Then, for each segment, the APCS automatically selects the allowable travel speed subjected to the dynamic constraint, and also the wire-feed rate according to a process model established in advance. Through the matching between the travel speed and the wire-feed rate, a uniform bead morphology among different segments is achieved. Experiments were conducted on a gantry robot using the Cold Metal Transfer (CMT) process, controlled by a self-developed computer numerical control (CNC) system, validating the efficacy of the proposed scheme.

Keywords Additive manufacturing · Wire and arc additive manufacturing · Adaptive process control · Dynamic constraint · Sharp corner · Complex-shaped component

1 Introduction

Additive manufacturing (AM), also known as layered manufacturing or 3D printing, has brought significant changes to the manufacturing industry. Contrary to conventional subtractive manufacturing where materials are removed, AM fabricates parts by joining materials together layer by layer, thus offering various benefits like limitless freedom in design, short production cycle and high material utilization [1–3]. Recently, with increasing demands from aerospace, automobile and marine, a lot of efforts in AM area have been put on fabricating functional metallic components that possess high geometrical complexity and are difficult or expensive to fabricate using conventional subtractive manufacturing.

Metallic AM technologies can be broadly categorized depending on how the feedstock is supplied (powder bed, powder-feeding and wire-feeding) and which energy source is selected (electron beam, laser and welding arc) [4]. Wire and arc additive manufacturing (WAAM), combining wire-feeding and welding arc, has drawn increasing research interest in recent years. Its deposition rate can reach up to 50–130 g/min, compared to 2–10 g/min in laser- or electron beam-based processes, which makes it highly competitive in fabricating medium- to large-scale metal components [5–7]. Besides, it offers other various benefits such as environmental friendliness, low equipment and material cost and strong bounding strength of materials.

✉ Shujun Chen
sjchen@bjut.edu.cn

Fang Li
lif@bjut.edu.cn

[1] College of Mechanical Engineering and Applied Electronics Technology, Beijing University of Technology, Beijing 100124, China

[2] Engineering Research Center of Advanced Manufacturing Technology for Automotive Components-Ministry of Education, Beijing University of Technology, Beijing 100124, China

Despite the above benefits, the WAAM technology has not yet matured due to a number of inherent technical challenges [8]. This paper mainly focuses on the issue of poor corner accuracy that is commonly encountered when fabricating complex-shaped components. It is known that the bead morphology of WAAM is quite sensitive to the fluctuation of its process parameters such as travel speed. As reported in Ref. [9], the bead width varies from 6.83 to 11.76 mm and the bead height from 2.17 to 3.8 mm for different travel speeds in gas metal arc welding (GMAW). Therefore, in order to achieve a uniform bead morphology along the tool-path, it is crucial to maintain a constant travel speed all through during the deposition process. Nevertheless, this requirement is always violated in practice on account of the welding robot's dynamic constraint. When sharp corners with high curvatures are encountered, the welding robot has to slow down such that the centripetal acceleration stays below the allowable value, or else excessive mechanical vibration may occur [10, 11]. The consequence is excessive fillings (i.e. humps), which not only increase the required post processing, but also degrade the quality of the subsequent layers. More seriously, the deposition process must be terminated when the accumulated errors in the build direction become too large.

The necessity of constant speed control in other AM processes has been confirmed by several previous studies. Ref. [12] proposes a tracking feedforward compensator and a look-ahead trajectory planning algorithm for the fused deposition (FD) process, which allows the liquefier-head subsystem to move with a constant speed as much as possible. Ref. [13] combines linear segments with parabolic blends (LSPBs) and minimum time trajectory (MTT) planning algorithms for the aerosol printing process also for a constant speed during printing. Ref. [14] proposes an original path planning algorithm based on Bézier curves aimed at ensuring a constant speed along the path with very slight oscillations. Ref. [15] proposes a level-set-based optimization method to generate contour parallel deposition path for the material extrusion-based additive manufacturing that is capable to reduce the number of sharp corners or high-curvature segments. However, none of them can completely avoid the drop of the travel speed around sharp corners. Ref. [16] proposes a novel technique called variable powder flow rate control (VPFRC) for the laser metal deposition process, which utilizes a non-constant reference powder flow rate trajectory to account for the change in travel speed, thereby maintaining a constant powder deposition per unit length for a more uniform track morphology. In Ref. [17] where fused filament fabrication (FFF) is studied, the tangential speed along the path is smoothed and optimized first, and then, the extrusion rate is controlled proportional to this speed while keeping a desirable temperature, thereby leading to more uniform material deposition at sharp corners. However, these techniques are not directly applicable to WAAM because metal wire and metal powder/plastic have different response characteristics.

To overcome the above difficulty, an adaptive process control scheme (APCS) aiming at guaranteeing a uniform bead morphology while still respecting the dynamic constraint is proposed for WAAM in this paper. Since it is difficult to maintain a constant travel speed along the entire tool-path, the APCS divides the tool-path into several segments depending on whether they contain sharp corners, and then determines the allowable travel speed of each segment separately subjected to the dynamic constraint. Though different segments may have different travel speeds, it is still possible to achieve a uniform bead morphology among different segments through adjusting the wire-feed rate adaptively. Through this way, the two goals, i.e. smooth mechanical movement and uniform bead morphology, can be realized simultaneously. The rest of this paper is organized as follows. Section 2 will detail the development of the APCS. Section 3 will validate the APCS through experiments conducted on a gantry robot based on the Cold Metal Transfer (CMT) process. Section 4 will conclude this paper.

2 Development of the APCS

The proposed APCS consists of five main modules: tool-path representation, sharp corner identification, tool-path segmentation, travel speed determination and wire-feed rate determination. These modules will be introduced in detail below.

2.1 Tool-path representation

The tool-path used in the APCS is based on non-uniform rational B-Spline (NURBS), instead of traditional small line segments. NURBS has become a standard interface between CAD/CAM/CNC systems, which is especially suitable for AM because it (1) avoids frequent and abrupt change of the motion direction and therefore allows higher and smoother travel speed, (2) represents very complex shapes with small program codes and (3) offers an exact uniform representation of analytical shapes as well as free-form parametric curves and surfaces [10, 11].

A general form of a NURBS curve is defined as follows:

$$C(u) = \frac{\sum_{i=0}^{n} N_{i,p}(u)\omega_i P_i}{\sum_{i=0}^{n} N_{i,p}(u)\omega_i} \tag{1}$$

where $\{P_i\}$ are the control points with a total number of $n+1$, $\{\omega_i\}$ are the corresponding weights of $\{P_i\}$ and p is the degree of the NURBS curve. $\{N_{i,p}(u)\}$ are the p_{th}-degree B-spline basis functions defined on the non-decreasing knot vector $U = \{u_0, u_1, \ldots, u_{n+p+1}\}$. The basis function is recursively defined as:

$$\begin{aligned} N_{i,0}(u) &= \begin{cases} 1 & u_i \le u \le u_{i+1} \\ 0 & otherwise \end{cases} \\ N_{i,p}(u) &= \frac{u-u_i}{u_{i+p}-u_i} N_{i,p-1}(u) + \frac{u_{i+p+1}-u}{u_{i+p+1}-u_{i+1}} N_{i+1,p-1}(u) \end{aligned} \tag{2}$$

A test tool-path with a trident shape based on NURBS is created for illustration, as shown in Fig. 1. Similar tool-paths can be found in several previous works [18, 19]. C_0 is designated as the starting point. C_1, C_2, C_3, C_4 and C_5 are the candidates of sharp corners. Only a few parameters are required to represent this complex shape as follows:

Control points (P_i): [0 0], [45 90], [7 48], [0 78], [−7 48], [−45 90], [0 0]

Weights (ω_i): {1 1 1 1 1 1 1}

Knots vector (U): {0, 0, 0, 0.2, 0.4, 0.6, 0.8, 1.0, 1.0, 1.0}

2.2 Sharp corner identification

This module aims to identify sharp corners on the tool-path that could lead to the drop of the travel speed. According to the dynamic constraint, whether a corner belongs to a sharp corner depends on whether its corresponding centripetal acceleration exceeds the maximum allowable value.

The centripetal acceleration A_{cen} when $u = u_i$ is calculated by multiplying the commanded travel speed V_{cmd} squared by the curvature $\kappa(u_i)$:

$$A_{\text{cen}}(u_i) = V_{\text{cmd}}^2 \kappa(u_i) \tag{3}$$

which implies that the higher the curvature is, the larger the centripetal acceleration becomes.

By substituting the maximum allowable acceleration $A_{\max}$ into Eq. (3), the threshold value κ_{thr} for identifying sharp corners is determined as follows:

$$\kappa_{\text{thr}} = \frac{A_{\max}}{V_{\text{cmd}}^2} \tag{4}$$

Any corner with its curvature being larger than κ_{thr} is identified as a sharp corner. For a NURBS-based tool-path expressed by Eq. (1) and (2), the curvature $k(u_i)$ can be calculated as [9, 10]:

$$\kappa(u_i) = \frac{\left\| C'(u_i) \times C''(u_i) \right\|}{\left\| C'(u_i) \right\|^3} \tag{5}$$

where $C'(u_i)$ and $C''(u_i)$ represent the first and second derivatives of the curve, respectively.

For the test tool-path given in Fig. 1, the threshold value κ_{thr} and the curvature κ as a function of u are calculated based on Eq. (4) and Eq. (5), respectively, as shown in Fig. 2. The values of $A_{\max}$ and V_{cmd} are given in Table 2 in Section 3.2. It is clearly observed that only C_1, C_3 and C_5 belong to sharp corners among the five candidate corners.

2.3 Tool-path segmentation

This module aims to divide the tool-path into several segments depending on whether they contain sharp corners.

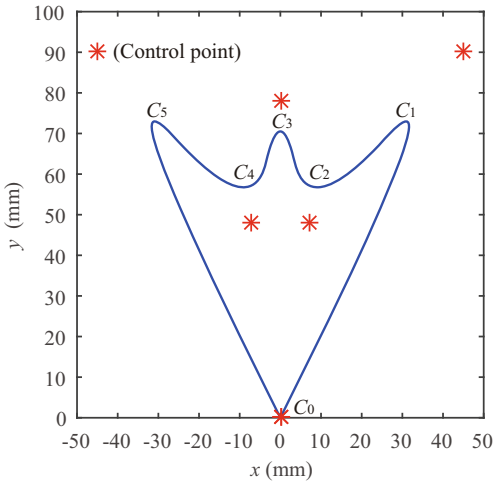

Fig. 1 Test tool-path based on NURBS and the control points

Two types of segments are defined: bumpy segment and smooth segment. A bumpy segment is defined as a collection of consecutive points around one sharp corner whose curvatures are higher than the threshold value. A smooth segment is defined as the consecutive points between two bumpy segments. Nevertheless, if the length of a bumpy segment is too short, the travel speed will decrease and then increase in a short time (see Section 2.4) and the wire-feed rate may not be able to respond in time to the rapid change of the travel speed. In such a case, this bumpy segment has to be extended and consequently the neighboring two smooth segments have to be shortened. In our study, the lower limit of a bumpy segment is set to 10 mm empirically to avoid frequent change of the travel speed. Based on the above principle, the test tool-path is

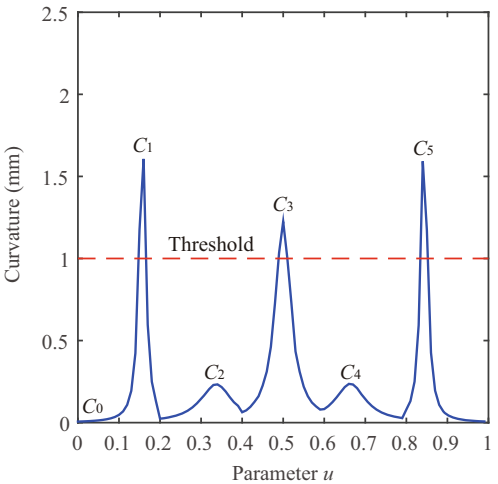

Fig. 2 Sharp corner identification by comparing the curvature and the threshold

divided into three bumpy segments and four smooth segments, as shown in Fig. 3.

2.4 Travel speed determination

This module aims to determine the allowable travel speed of each segment separately subjected to the dynamic constraint, and also smooth the transition between neighboring segments. The dynamic constraint demands that the centripetal acceleration A_{cen} in Eq. (3) should not exceed the maximum allowable value $A_{\max}$. Then, the allowable travel speed of each segment V_i (i denotes the number of the segment) should satisfy

$$V_i = \min\left\{\sqrt{\frac{A_{\max}}{\kappa_{i,\max}}}, V_{\text{cmd}}\right\} \tag{6}$$

where $\kappa_{i,\max}$ is the maximum curvature of the i-th segment.

When $\kappa_{i,\max} = \kappa_{\text{thr}}$, the two terms in the right hand of Eq. (6) are equal combining Eq. (4). In smooth segments where all the points have lower curvatures than the threshold value κ_{thr}, the allowable travel speed is determined by the second term, i.e.

$$V_{smooth} = V_{\text{cmd}} \tag{7}$$

In bumpy segments, however, some points have higher curvatures than κ_{thr}, and therefore the allowable travel speed is determined by the first term, i.e.

$$V_{bumpy} = \sqrt{\frac{A_{\max}}{\kappa_{i,\max}}} \tag{8}$$

which decreases with increasing curvature.

From Eqs. (7) and (8), we know that the travel speed maintains the commanded value in smooth segments and decreases in bumpy segments in accordance to the local maximum curvature. However, the sudden change of the travel speed at the junction between neighboring segments is undesirable. On the one hand, excessive mechanical vibration may occur because of infinite acceleration. On the other hand, the wire-feed rate is not able to respond in time to the sudden change of the travel speed. To deal with this problem, a simple S-shaped acceleration/deceleration (ACC/DEC) profile [20] is adopted to smooth the transition between neighboring segments. The ACC/DEC profiles from smooth to bumpy segments and from bumpy to smooth segment are determined by Eqs. (9) and (10), respectively. Particularly, the ACC/DEC transitions are equally split between bumpy and smooth segments.

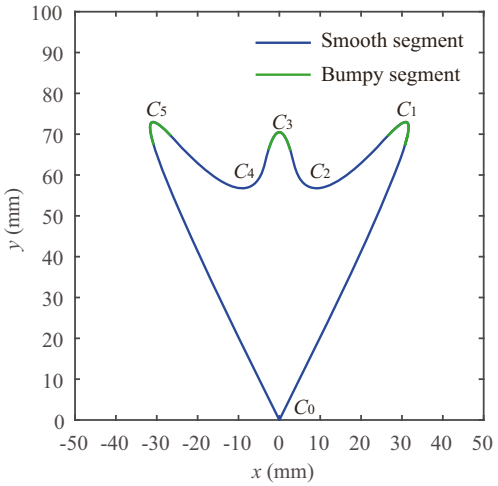

Fig. 3 Test tool-path divided into smooth segments and bumpy segments

$$\begin{cases} V_{Smooth\text{-}Bumpy} = V_{Smooth} + \frac{1}{2}J_{\max}t^2, & t \le \frac{dT}{2} \\ V_{Smooth\text{-}Bumpy} = V_{Smooth} - \frac{1}{4}J_{\max}dT^2 + J_{\max}dTt - \frac{1}{2}J_{\max}t^2, & \frac{dT}{2} < t \le dT \\ dT = 2\sqrt{(V_{Smooth} - V_{Bumpy})/J_{\max}} \end{cases} \tag{9}$$

$$\begin{cases} V_{Bumpy\text{-}Smooth} = V_{Bumpy} - \frac{1}{2}J_{\max}t^2, & t \le \frac{dT}{2} \\ V_{Bumpy\text{-}Smooth} = V_{Bumpy} + \frac{1}{4}J_{\max}dT^2 - J_{\max}dTt + \frac{1}{2}J_{\max}t^2, & \frac{dT}{2} < t \le dT \\ dT = 2\sqrt{(V_{Smooth} - V_{Bumpy})/J_{\max}} \end{cases} \tag{10}$$

where $J_{\max}$ denotes the maximum allowable jerk.

Combining Eqs. (7)–(10), the entire travel speed profile for the test tool-path is generated, as displayed in Fig. 4.

2.5 Wire-feed rate determination

In this section, a process model that relates two input variables (travel speed and wire-feed rate) and two output responses (bead width and bead height) is established, which is used to determine the required wire-feed rate of each segment that matches the corresponding travel speed for a uniform bead morphology. Such a model is nonlinear and therefore hard to be represented accurately with an analytical form. This paper adopts an artificial neural network (ANN) method, which has the capability to satisfactorily represent any arbitrary nonlinear model if the neural network is properly and sufficiently trained [21, 22]. For training purposes, nine sets of single-

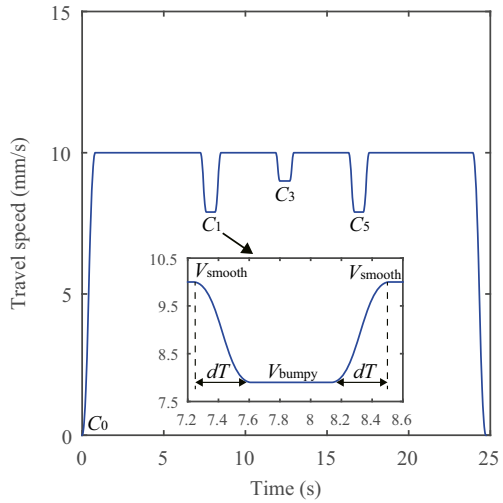

Fig. 4 Travel speed profile for the test tool-path

layer deposition experiments with different combinations of travel speed and wire-feed rate were conducted, which were determined based on a quadratic general rotary unitized design as shown in Table 1 (No. 1–No. 9). These data were normalized before training to ensure that each input parameter has the same contribution to the neural network. The details of the experimental setup and the measuring method will be introduced in Section 3.1. The training was performed using the MATLAB application tool. A neural network composed of one input layer, one hidden layer with eight neurons and one output layer was constructed. The transfer function for the hidden neurons was a tangent sigmoid function and for the output neurons was a linear function. The gradient descent back propagation algorithm was selected as the training function. In addition, the learning rate was set to 0.05, the training epochs were set to 5000 and the goal of the root mean square error (RMSE) was determined to be 1e-5. After the training was finished, four additional experiments were carried out to check the accuracy of the neural network, as given in Table 1 (No. 10–No. 13). The predicted bead height and bead width based on the neural work agree well with the experimental ones.

Based on the neural network, the bead width and the bead height as a function of the travel speed and the wire-feed rate are obtained, as intuitively displayed in Fig. 5 [22]. This figure enables to search the required wire-feed rate of each segment that matches the corresponding travel speed for a uniform bead morphology. In some cases, however, the required wire-feed rate may not exist. To solve this problem, we enlarge the search scope as shown in Eq. (11), which allows a small deviation of the bead width and the bead height from the target ones.

$$\begin{aligned} Width_{search} &\subset \left[Width_{target} - 0.2,\ \ Width_{target} + 0.2\right] \\ Height_{search} &\subset \left[Height_{target} - 0.1,\ \ Height_{target} + 0.1\right] \end{aligned} \tag{11}$$

Table 1 Experimental design matrix and the responses

No.	Travel speed (mm/s)	Wire-feed rate (m/min)	Bead width (mm)	Bead height (mm)
1	9.4	3.3	4.96	1.67
2	9.4	2.7	3.99	1.51
3	6.6	3.3	5.45	1.84
4	6.6	2.7	4.49	1.87
5	6.0	3.0	5.07	1.91
6	10.0	3.0	4.37	1.54
7	8.0	2.5	3.92	1.67
8	8.0	3.5	5.53	1.78
9	8.0	3.0	4.72	1.72
10	7.0	3.5	5.60	1.81
			5.71*	1.83*
11	8.0	3.3	5.10	1.75
			5.19*	1.70*
12	9.0	3.1	4.71	1.65
			4.98*	1.71*
13	10.0	2.9	4.21	1.51
			4.11*	1.46*

*Denotes the predicted data based on the neural network

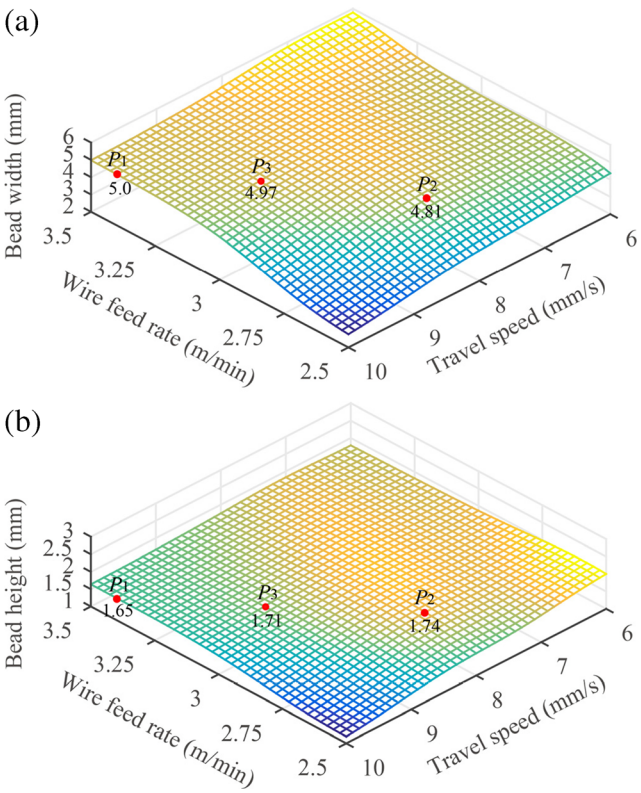

Fig. 5 Bead width and bead height as a function of travel speed and wire-feed rate

Then, the wire-feed rate profile for the test tool-path that matches the travel speed profile in Fig. 4 is obtained, as shown in Fig. 6. The transition between neighboring segments is also smoothed based on the S-shaped ACC/DEC profile. The smooth segments, the corners C_1/C_5 and the corner C_3 correspond to the process parameters at the points P_1, P_2 and P_3 in Fig. 5 respectively. We can see that the differences in bead width and bead height between different points are within the allowable range given in Eq. (11).

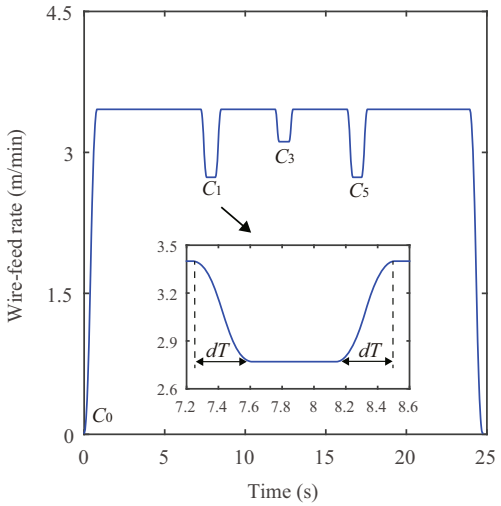

Fig. 6 Wire-feed rate profile for the test tool-path

3 Experiments

3.1 Experimental setup

The experimental setup consists of a three-axis gantry robot, a Fronius welding machine with the CMT process and a self-developed computer numerical control (CNC) system, as shown in Fig. 7. CMT, a GMAW variant based on a controlled dip transfer mode mechanism, has been investigated for its suitability for AM applications, providing high quality and spatter free deposition with low heat input and excellent reproducibility [23]. The CNC system has a master-slave framework. The master station, an embedded PC (CX1020, 1 GHz Intel® CPU, Beckhoff), was used to implement the proposed APCS. The slave stations were used to control the servomotors of the gantry robot through the EtherCAT protocol and communicate with the welding machine through the DeviceNet protocol. These high-speed protocols guaranteed good synchronism between the gantry robot and the welding machine such that the travel speed and the wire-feed rate could coordinate well. The wire material used in the experiments was aluminum alloy (4.8–5.2% Mg) with a diameter of 1.2 mm. The shielding gas was Ar at a flow rate of 15 L/min. The substrate had dimensions 100 mm × 100 mm × 5 mm. The CMT frequency was set to 70 Hz and the arc length was fixed to 10 mm.

3.2 Methods

Two experiments were carried out for comparison of the conventional process control scheme (CPCS) and the proposed APCS for the same tool-path given in Fig. 1. The key parameters for them are listed in Table 2. As is known, higher travel speed contributes to improving deposition efficiency and reducing heat input per unit length. However, a continued increase of the travel speed is impossible in practice, restricted by humping phenomenon. According to [24], for the CMT process, humping occurs when the travel speed exceeds 10 mm/s. Therefore, V_{cmd} was set to be 10 mm/s in this study. The commanded wire-feed rate W_{cmd} was set to 3.4 m/min to

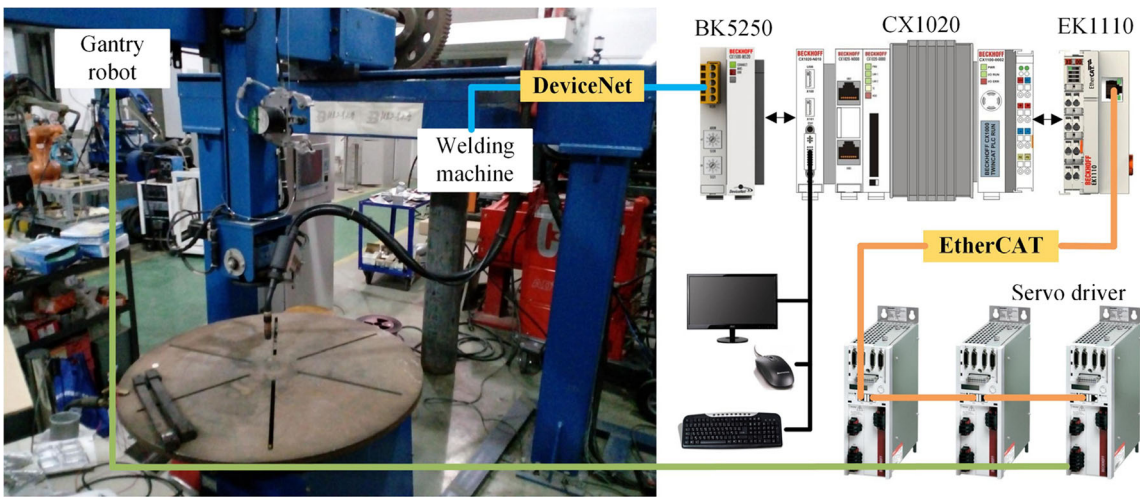

Fig. 7 Experimental setup and the CNC system

Table 2 Key parameters for the CPCS and the APSC

Parameter	Symbol	Value
Commanded travel speed	V_{cmd}	10 mm/s
Commanded wire-feed rate	W_{cmd}	3.4 m/min
Maximum allowable acceleration	A_{max}	100 mm/s^2
Maximum allowable jerk for the APCS	J_{max}	50 mm/s^3
Maximum allowable jerk for the CPCS	J_{max1}	1000 mm/s^3

obtain a bead width of 5 mm according to Fig. 5 (P_1). The corresponding welding current was 54 A. Different axes may provide different acceleration due to the difference in motor torque, load mass, frictional force, etc., and the maximum allowable acceleration A_{max} should be determined by the "slowest" axis. After evaluating the dynamics performances of the three axes, A_{max} was determined to be 100 mm/s^2. The maximum allowable jerk J_{max} for the APCS was much smaller than that for the CPSC. The aim is to increase the transition time between neighboring segments according to Eqs. (9) and (10) to facilitate the adjustment of the wire-feed rate. A total of 16 layers were deposited in the two experiments.

Based on the parameters in Table 2, the travel speed profile generated by the CPCS is shown in Fig. 8a. It is based on a classical interpolation algorithm, which also takes the centripetal acceleration constraint into account [10], but demands a steeper drop of the travel speed around sharp corners than the APCS. Besides, the wire-feed rate stays unchanged all through. Fig. 8b shows the travel speed and wire-feed rate profiles generated by the APCS, which have already been presented above (Fig. 4 and Fig. 6). The differences between the CPCS and the APCS are clearly seen from Fig. 8.

3.3 Results

Figure 9 compares the obtained near net shapes in the two experiments. Tremendous dimension errors in both the horizontal and vertical directions, i.e. humps, were observed around the corners C_1, C_3 and C_5 in the first experiment (CPCS), which were directly due to the steep drop of the travel speed as seen in Fig. 8a. Besides, C_1 and C_5 had larger curvature than C_3 and their corresponding dimension errors were larger. This is because higher curvature caused larger drop of the travel speed and therefore more material was deposited. For the corners C_2 and C_4 with lower curvature than the threshold value, no noticeable dimension errors were observed. In the second experiment (APCS), in contrast, the actual bead morphology approximated to the target one well with satisfactory corner accuracy, regardless of the fluctuation of the travel speed. This implies that the travel speed and the wire-feed rate matched pretty well based on the established process model. As a result, the required post processing is minimized and therefore less material is wasted. It should also be pointed out that the APCS needed a little longer build time than the CPCS because the average travel speed was lower. However, the small increase of the build time is acceptable in practice.

Figure 10 compares the measurement results in the two experiments with the aid of a laser profile scanner (HG-C1030, Panasonic, 0.01 mm repeatable precision), and Table 3 summarizes the statistical data. A total of 30 measurement points evenly spaced along the tool-path were selected. The maximum deposition height error after depositing 16 layers reached 4.4 mm when the CPCS was

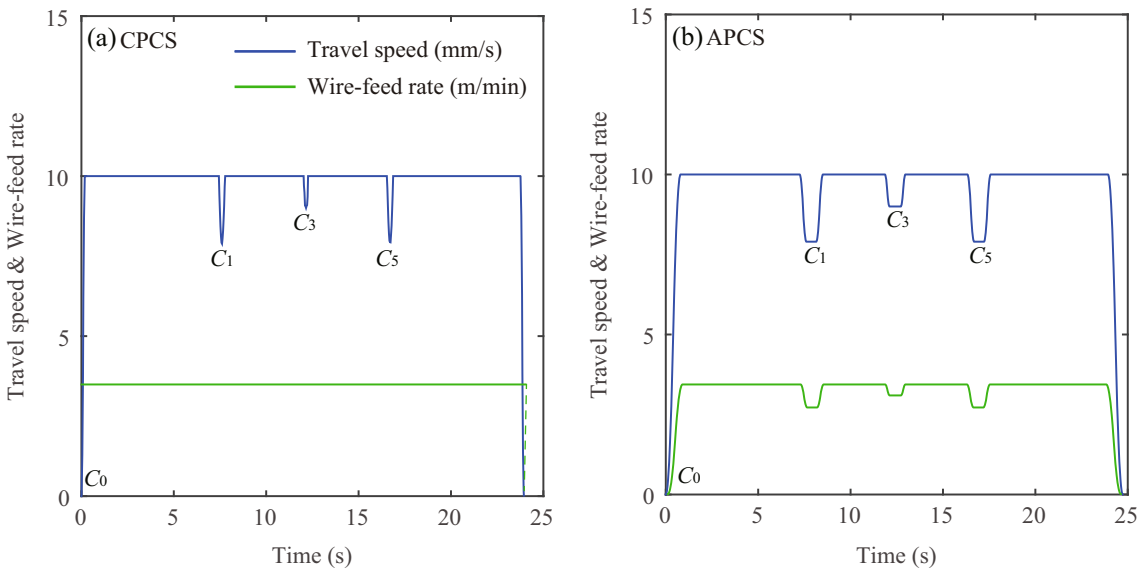

Fig. 8 Travel speed and wire-feed rate comparison between the CPCS and the APCS

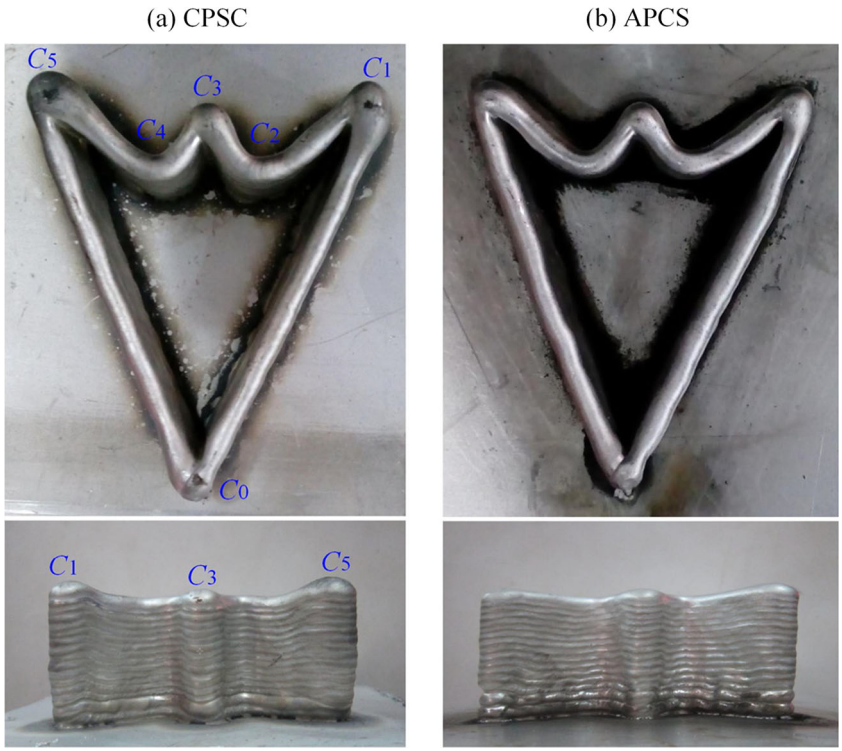

Fig. 9 Near net shape comparison between the CPCS and the APCS

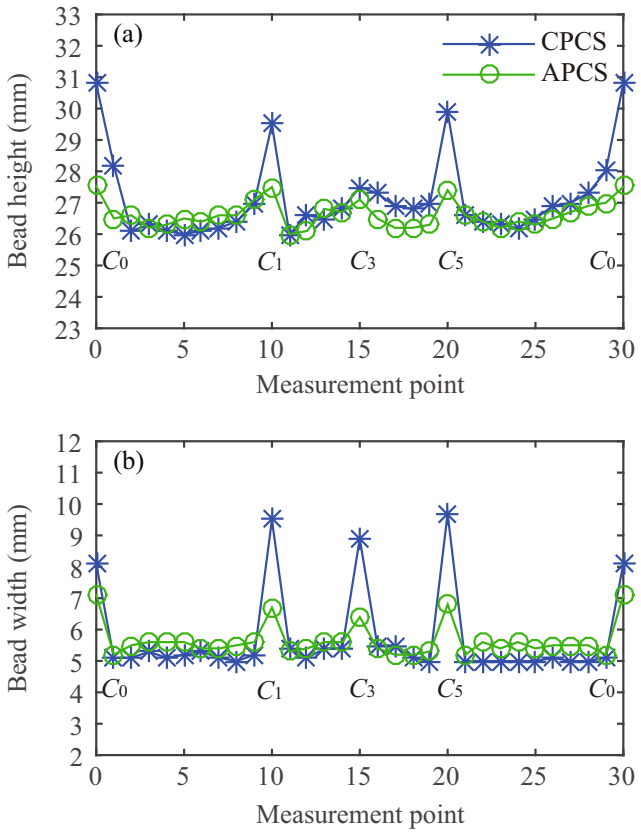

Fig. 10 Bead width and bead height comparison between the CPCS and the APCS

implemented. In such a situation, the deposition process had to be terminated because the torch was too close to the upper surface of the deposited material. When the APCS was implemented, the maximum dimension errors in the horizontal and vertical directions were reduced significantly by 55 and 75% respectively. However, the dimension errors in the two directions still existed, not only at bumpy segments, but also at smooth segments. Several reasons may explain this. First, the wire-feed rate may not match perfectly with the travel speed at bumpy segments (see Eq. (11)). Secondly, the small corner radius may lead to the bead to curl up on itself. This may be only solved by re-planning the tool-path taking the bead width into account [15]. Thirdly, the process model was developed based on single-layer deposition experiments, and the bead dimensions of upper layers may deviate a little from the first layer due to their difference in heat dissipation condition.

Table 3 Statistical data of the bead dimension errors in the experiments

	Bead width error (mm)			Deposition height error/16 layers (mm)		
	Maximum	Mean	Standard	Maximum	Mean	Standard
CPSC	4.7	0.75	1.42	4.4	0.76	1.34
APCS	2.1	0.66	0.55	1.1	0.23	0.43

4 Conclusions

This paper proposes an adaptive process control scheme (APCS) to solve the issue of poor corner accuracy that is commonly encountered when fabricating complex-shaped components in WAAM. APCS divides the tool-path into several segments depending on whether they contain sharp corners, and optimizes the travel speed and the wire-feed rate within each segment according to the dynamic constraint and the process model respectively. Through this way, the two goals, i.e. smooth mechanical movement and uniform bead morphology, can be realized simultaneously. Experimental results show that the maximum dimension errors in the horizontal and vertical directions are reduced by 55 and 75% respectively compared to the conventional control scheme. The improved uniformity of the bead morphology contributes to not only minimizing the required post processing, but also maintaining a constant torch-to-workpiece distance. Future work will focus on incorporating the APCS into the path planning algorithm dedicated to the WAAM process.

Funding information This paper was supported by the National Natural Science Foundation of China (no. 51475009) and China Postdoctoral Science Foundation (no. 2017 M610726).

References

1. Gao W, Zhang Y, Ramanujan D, Ramani K, Chen Y, Williams CB, Wang CCL, Shin YC, Zhang S, Zavattieri PD (2015) The status, challenges, and future of additive manufacturing in engineering. Comput Aided Des 69:65–89. https://doi.org/10.1016/j.cad.2015.04.001
2. Thompson MK, Moroni G, Vaneker T, Fadel G, Campbell RI, Gibson I, Bernard A, Schulz J, Graf P, Ahuja B, Martina F (2016) Design for additive manufacturing: trends, opportunities, considerations, and constraints. CIRP Ann-Manuf Techn 65(2):737–760. https://doi.org/10.1016/j.cirp.2016.05.004
3. Chen L, He Y, Yang Y, Niu S, Ren H (2017) The research status and development trend of additive manufacturing technology. Int J Adv Manuf Technol 89(9–12):3651–3660. doi: https://doi.org/10.1007/s00170-016-9335-4
4. Frazier WE (2014) Metal additive manufacturing: a review. J Mater Eng Perform 23(6):1917–1928. https://doi.org/10.1007/s11665-014-0958-z
5. Bai JY, Fan CL, Lin SB, Yang CL, Dong BL (2016) Effects of thermal cycles on microstructure evolution of 2219-Al during GTA-additive manufacturing. Int J Adv Manuf Technol 87(9–12):2615–2623. https://doi.org/10.1007/s00170-016-8633-1
6. Ding D, Pan Z, Cuiuri D, Li H (2015) Wire-feed additive manufacturing of metal components: technologies, developments and future interests. Int J Adv Manuf Technol 81(1–4):465–481. https://doi.org/10.1007/s00170-015-7077-3
7. Li F, Chen S, Shi J, Tian H, Zhao Y (2017) Evaluation and optimization of a hybrid manufacturing process combining wire arc additive manufacturing with milling for the fabrication of stiffened panels. Appl Sci 7(12):1233. doi:https://doi.org/10.3390/app7121233
8. Urbanic RJ, Hedrick RW, Burford CG (2017) A process planning framework and virtual representation for bead-based additive manufacturing processes. Int J Adv Manuf Technol 90(1–4):361–376. https://doi.org/10.1007/s00170-016-9392-8
9. Xiong J, Zhang G, Hu J, Wu L (2014) Bead geometry prediction for robotic GMAW-based rapid manufacturing through a neural network and a second-order regression analysis. J Intell Manuf 25(1):157–163. https://doi.org/10.1007/s10845-012-0682-1
10. Liu X, Ahmad F, Yamazaki K, Mori M (2005) Adaptive interpolation scheme for NURBS curves with the integration of machining dynamics. Int J Mach Tool Manu 45(4):433–444. https://doi.org/10.1016/j.ijmachtools.2004.09.009
11. Annoni M, Bardine A, Campanelli S, Foglia P, Prete CA (2012) A real-time configurable NURBS interpolator with bounded acceleration, jerk and chord error. Comput Aided Des 44(6):509–521. doi: https://doi.org/10.1016/j.cad.2012.01.009
12. Bouhal A, Jafari MA, Han WB, Fang T (1999) Tracking control and trajectory planning in layered manufacturing applications. IEEE T Ind Electron 46(2):445–451. https://doi.org/10.1109/41.753784
13. Thompson B, Yoon H (2014) Efficient path planning algorithm for additive manufacturing systems. IEEE T Comp Pack Man 4(9):1555–1563. https://doi.org/10.1109/TCPMT.2014.2338791
14. Giberti H, Sbaglia L, Urgo M (2017) A path planning algorithm for industrial processes under velocity constraints with an application to additive manufacturing. J Manuf Syst 43:160–167. doi: https://doi.org/10.1016/j.jmsy.2017.03.003
15. Jin Y, Du J, Ma Z, Liu A, He Y (2017) An optimization approach for path planning of high-quality and uniform additive manufacturing. Int J Adv Manuf Technol 92(1–4):651–662. https://doi.org/10.1007/s00170-017-0207-3
16. Tang L, Ruan J, Landers RG, Liou F (2008) Variable powder flow rate control in laser metal deposition processes. J Manuf Sci E 130(4):95–102. https://doi.org/10.1115/1.2953074
17. Ertay DS, Yuen A, Altintas Y (2017) Synchronized material deposition rate control with path velocity on fused deposition machines. Addit Manuf (in press) 19:205–213. https://doi.org/10.1016/j.addma.2017.05.011
18. Lin MT, Tsai MS, Yau HT (2007) Development of a dynamics-based NURBS interpolator with real-time look-ahead algorithm. Int J Mach Tool Manu 47(15):2246–2262. https://doi.org/10.1016/j.ijmachtools.2007.06.005
19. Beudaert X, Lavernhe S, Tournier C (2012) Feedrate interpolation with axis jerk constraints on 5-axis NURBS and G1 tool path. Int J Mach Tool Manu 57(3):73–82. https://doi.org/10.1016/j.ijmachtools.2012.02.005
20. Liu M, Huang Y, Yin L, Guo JW, Shao XY, Zhang GJ (2014) Development and implementation of a NURBS interpolator with smooth feedrate scheduling for CNC machine tools. Int J Mach Tool Manu 87:1–15. https://doi.org/10.1016/j.ijmachtools.2014.07.002
21. Huang W, Kovacevic R (2011) A neural network and multiple regression method for the characterization of the depth of weld penetration in laser welding based on acoustic signatures. J Intell Manuf 22(2):131–143. https://doi.org/10.1007/s10845-009-0267-9
22. Ding D, Pan Z, Cuiuri D, Li H, Duin SV, Larkin N (2016) Bead modelling and implementation of adaptive MAT path in wire and arc additive manufacturing. Robot Cim-Int Manuf 39:32–42. https://doi.org/10.1016/j.rcim.2015.12.004
23. Almeida PMS, Williams S (2010) Innovative process model of Ti–6Al–4V additive layer manufacturing using cold metal transfer (CMT). Proccedings of the International Solid Freeform Fabrication Symposium:25–36
24. Adebayo A, Mehnen J, Tonnellier X (2013) Limiting travel speed in additive layer manufacturing. Trends in Welding Research: Proceedings of the 9th International Conference:1038–1044